

Eulerian indicators under continuously varying conditions

Kevin L. McIlhenny and Stephen Wiggins

Citation: *Phys. Fluids* **24**, 073601 (2012); doi: 10.1063/1.4732152

View online: <http://dx.doi.org/10.1063/1.4732152>

View Table of Contents: <http://pof.aip.org/resource/1/PHFLE6/v24/i7>

Published by the [American Institute of Physics](#).

Related Articles

Cartography of high-dimensional flows: A visual guide to sections and slices

Chaos **22**, 047506 (2012)

Convection and reaction in a diffusive boundary layer in a porous medium: Nonlinear dynamics

Chaos **22**, 037113 (2012)

Interactions between active particles and dynamical structures in chaotic flow

Phys. Fluids **24**, 091902 (2012)

Chaotic dynamics and oxygen transport in thin films of aerotactic bacteria

Phys. Fluids **24**, 091701 (2012)

Spectral analysis of mixing in chaotic flows via the mapping matrix formalism: Inclusion of molecular diffusion and quantitative eigenvalue estimate in the purely convective limit

Phys. Fluids **24**, 073603 (2012)

Additional information on Phys. Fluids

Journal Homepage: <http://pof.aip.org/>

Journal Information: http://pof.aip.org/about/about_the_journal

Top downloads: http://pof.aip.org/features/most_downloaded

Information for Authors: <http://pof.aip.org/authors>

ADVERTISEMENT



**Running in Circles Looking
for the Best Science Job?**

Search hundreds of exciting
new jobs each month!

<http://careers.physicstoday.org/jobs>

physicstodayJOBS



Eulerian indicators under continuously varying conditions

Kevin L. McIlhany^{1,a)} and Stephen Wiggins^{2,b)}

¹*Physics Department, U. S. Naval Academy, Stop 9c, 572c Holloway Rd., Annapolis, Maryland 21402-5002, USA*

²*School of Mathematics, University of Bristol, University Walk, Bristol BS8 1TW, United Kingdom*

(Received 27 January 2012; accepted 31 May 2012; published online 9 July 2012)

In this paper, we extend the notion of Eulerian indicators (EIs) for predicting Lagrangian mixing behavior previously developed for blinking flows to the continuous time setting. We apply the EIs to a study of mixing in a kinematic model of a time-dependent double-gyre with five different time dependencies—sinusoidal, sawtooth, square wave, triangular, and noise (which is constructed so that it is also periodic in time). Each of the five velocity fields is described by two parameters; the strength of the time dependence (ϵ) and the period (T). Based on a trajectory based quality of mixing diagnostic (Danckwerts' normalized variance of concentration) we find that noisy time dependence has the largest region of good mixing in the parameter space and triangular time dependence has parameter values corresponding to the most complete and fastest mixing. These Lagrangian based predictions are confirmed by the EIs (product of the transversality and mobility). Although not every feature of the mixing behavior is captured by EIs, we show that they do in general predict the regions in the parameter space under consideration that correspond to good mixing. Moreover, the EIs offer a factor of 100 computational advantage in exploring the parameter space in comparison with the trajectory based mixing diagnostic.

© 2012 American Institute of Physics. [<http://dx.doi.org/10.1063/1.4732152>]

I. INTRODUCTION

Over the past 30 years many new insights into Lagrangian transport and mixing have been obtained through the mathematical framework of dynamical systems theory. Nevertheless, it is important to realize that the key elements of the physical picture of the kinematics of fluid mixing stretching and folding were articulated years before dynamical systems theory entered the picture. In particular, Reynolds,¹ Eckart,² and Danckwerts^{3,4} gave very clear descriptions of the kinematics of the stretching and folding process in fluids. Ottino⁵ has made the point that even though the physical picture of the kinematics of stretching and folding was understood, progress in implementing this picture in the analysis of particular fluid flows did not come until there was wide acceptance and use of a mathematical framework that allowed a predictive and computational realization of the kinematic stretching and folding paradigm, and this mathematical framework is dynamical systems theory.

The dynamical systems approach to transport in fluids is inherently Lagrangian since the geometrical framework of dynamical systems theory, as described first by Poincaré, is concerned with all possible motions of fluid particle trajectories and how they are related. Here, we distinguish the Eulerian and Lagrangian points of view of fluid mechanics in a very operational sense. By Eulerian we refer to the velocity field that is a function of (fixed) locations in space, and time. By Lagrangian we refer to the trajectories generated by the ordinary differential equation defined by the velocity field. This naturally leads to mathematical descriptions of experimentally visualized structures such as transport routes, transport barriers, and regions of good and poor mixing. Consequently, the

a) mcilhany@usna.edu.

b) s.wiggins@bristol.ac.uk.

success of the dynamical systems approach to the description and analysis of Lagrangian transport has been such that transport and mixing are almost exclusively viewed in this Lagrangian setting.

Certainly transport and mixing are archetypical Lagrangian phenomena since they are fundamentally concerned with the motion of fluid particles and their relative displacements with respect to each other. Nevertheless, it is important to keep in mind that particles move as a result of the velocity field, and the characteristics of the velocity field, therefore must play a role in the Lagrangian processes of transport and mixing. Stating this slightly differently, Eulerian features of the velocity field certainly play a role in determining the nature of transport and mixing. Is it possible to predict which Eulerian characteristics lead to specific Lagrangian behavior?

On first thinking along these lines, there might appear to be little hope for progress. After all, the particle trajectories are solutions of the ordinary differential equation defined by the velocity field and, from experience, one generally has to work to obtain the solutions of a (typically) nonlinear differential equation. Nevertheless, the physical insight obtained from careful studies of experiments of mixing phenomena coupled with the geometric theory of dynamical systems theory offers some hope.

In early experiments on chaotic advection Ottino⁶ observed that streamline crossing appeared to promote good mixing. More recently, Villermaux, Stroock, and Stone⁷ observed that transversely oriented shears appeared to promote good mixing in certain channel or duct flows. It was noted in Refs. 8 and 9 that these Eulerian characteristics are embodied in a class of two-dimensional area preserving maps that are referred to as linked twist maps (LTMs) in the dynamical systems literature.¹⁰ Briefly, in fluid mechanics terminology the “linked” in the name LTM refers to streamline crossing and the “twist” in the name LTM refers to shear. Mathematically, LTMs are remarkable dynamical systems since, for certain conditions on the nature of the “linkage” and the “twist,” it is possible to insure (ergodic theoretic) mixing on regions of non-zero area. Precise statements of these theorems can be found in Ref. 10, but we do not give them here since they are not important for the focus of this paper.

The LTM framework serves as the basis for certain paradigm blinking flows exhibiting chaotic mixing, such as the Aref blinking vortex flow¹¹ (“blinking in time”) and the partitioned pipe mixer¹² (“blinking in space”, i.e., by this we mean that the flow is steady, three-dimensional, and spatially periodic and the particle trajectories are studied by considering a two-dimensional mapping between a cross-section transverse to the axial direction of flow to “itself” (by spatial periodicity), details of this construction, along with the relation to LTMs and examples, can be found in Ref. 10). These particular blinking flows were studied in Ref. 13, where, motivated by the LTM framework, Eulerian indicators (EIs) were first developed to quantify the notion of streamline crossing and transversely oriented shears. Eulerian indicators were further developed and applied to models of the staggered herringbone mixer (SHM) developed by Stroock *et al.*¹⁴ in Refs. 15 and 16. In the latter paper a new EI, mobility, was developed in an attempt to quantify the amount of fluid flowing with a high degree of transport. There it was found that the product of the transversality and mobility agreed with the regions of best mixing predicted by the variance of concentration. In this case, the EIs afforded a substantial computational advantage over the trajectory based quantifier of mixing. This allowed a more complete exploration of the parameter space for the model of the SHM and led to the discovery of a new optimal mixing configuration for the SHM that had previously been unknown.

In this paper, we apply the methodology of EIs to a new setting: two-dimensional, continuously time varying velocity fields. In particular, the measure of streamline crossing (referred to as transversality) developed in Ref. 13 is generalized to this setting. The so-called “mobility,” developed in Ref. 16, immediately generalizes to this setting. A new EI is introduced that allows us to characterize the rate of change of a continuously time varying velocity field, which we refer to as the relative rate of change (RROC). The RROC is closely related to the continuous time definition of mobility.

We emphasize that presently there are no rigorous mathematical theorems, analogous to the LTM theorems, that relate the EIs to a quantitative mixing characteristic (e.g., ergodic theoretic strong mixing on a set of non-zero area). At this point they show a correlation between certain Eulerian properties in the flow domain and the “quality of mixing” (as defined by the decay of the variance of concentration). In some sense, the situation is similar to the Lagrangian situation of demonstrating the presence of Smale horseshoes in flows and its consequences for mixing. The existence of the Smale

horseshoe does not provide a quantitative description of the mixing properties in the region where the Smale horseshoe exists. However, it can often be correlated with “good mixing” conditions, as confirmed by numerical simulation of particle trajectories, see, e.g., Ref. 5.

The EIs are applied to a study of mixing in the time-dependent double-gyre model of Shadden *et al.*,¹⁷ who consider a sinusoidally time varying velocity field. In addition, we consider four additional time dependencies sawtooth, square wave, triangular, and noise. Each velocity field is characterized by two parameters the period, T , and the strength of the time dependence, ϵ . A technique, using the RROC, is introduced that allows us to create a periodic noisy signal which allows for a comparison with the other four T -periodic velocity fields.

A particle trajectory based diagnostic, the normalized variance of concentration described in Refs. 3 and 4, is used to assess the mixing efficiency of the five models. The variance of concentration is computed for 100 time units in all cases, and then fit to a two parameter, exponentially decaying function (in time), previously described in Refs. 15 and 16. The two parameters are the lifetime (τ) and the amount of unmixed fluid (the bias, b). Hence, the best mixing occurs when τ and b are the smallest. Based on the tau-bias fits, we find that triangular time dependence has parameter values corresponding to the most complete and fastest mixing. However, we find that noisy time dependence has the largest region of good mixing in the $T - \epsilon$ parameter space. These particle trajectory based predictions are confirmed by the EIs (product of the transversality and mobility). Moreover, the EIs offer a factor of 100 computational advantage in exploring the parameter space in comparison with the particle trajectory based mixing diagnostic. This latter point is important to emphasize. Particle trajectory based diagnostics for mixing require the generation of many fluid particle trajectories for a long time. EIs do not require the generation of particle trajectories. In that sense, EIs are *predictive* and particle trajectory based diagnostics are *retrodictive*. The point is emphasized in Refs. 13, 15, and 16.

This paper is organized as follows. In Sec. II we describe the kinematic model for the time-dependent double-gyre and the five different types of time dependencies. In Sec. III we develop the EIs for continuously time varying velocity fields. In Sec. IV we describe the particle based measure of the quality of mixing that we use the normalized variance of concentration as originally described in Refs. 3 and 4. In Sec. V we describe the results. In Sec. V C we consider the computational efficiency of EIs as compared with trajectory based Lagrangian metrics for assessing mixing. In Sec. VI we state our conclusions. In Appendix A we describe how we construct a periodic, but noisy time-dependent function. In Appendix B we discuss our characteristic time scale for the time-dependent double-gyre flow.

II. KINEMATIC MODEL FOR A DOUBLE-GYRE FLOW

In this paper, we will use the model of a time-dependent double-gyre flow considered in Ref. 17,

$$\psi(x, y, t) = A \sin(\pi f(x, t)) \sin(\pi y), \quad (1)$$

$$f(x, t) = a(t)x^2 + b(t)x, \quad (2)$$

$$a(\omega t) = \epsilon \sin(\omega t), \quad (3)$$

$$b(\omega t) = 1 - 2a(\omega t). \quad (4)$$

The domain of the flow is $\mathcal{D} \equiv \{(x, y) \in \mathbb{R}^2 \mid 0 \leq x \leq 2, 0 \leq y \leq 1\}$. More general time dependence can be considered in this model by replacing the $\sin(\omega t)$ term in $a(\omega t)$ with a function having a different time dependence. In particular, in this paper we will consider five different time dependencies: sinusoidal (the same as in Ref. 17, which will serve as a reference), square wave (which corresponds to a blinking flow), sawtooth, triangular, and noise. How noise is applied will be discussed in Appendix A.

The parameter space that we consider is maximal distance either gyre can be displaced from the center, ϵ , and the period ($T = \frac{2\pi}{\omega}$) over the range $0.0 \leq \epsilon \leq 0.50$ and $1.0 \leq T \leq 20.0$. The

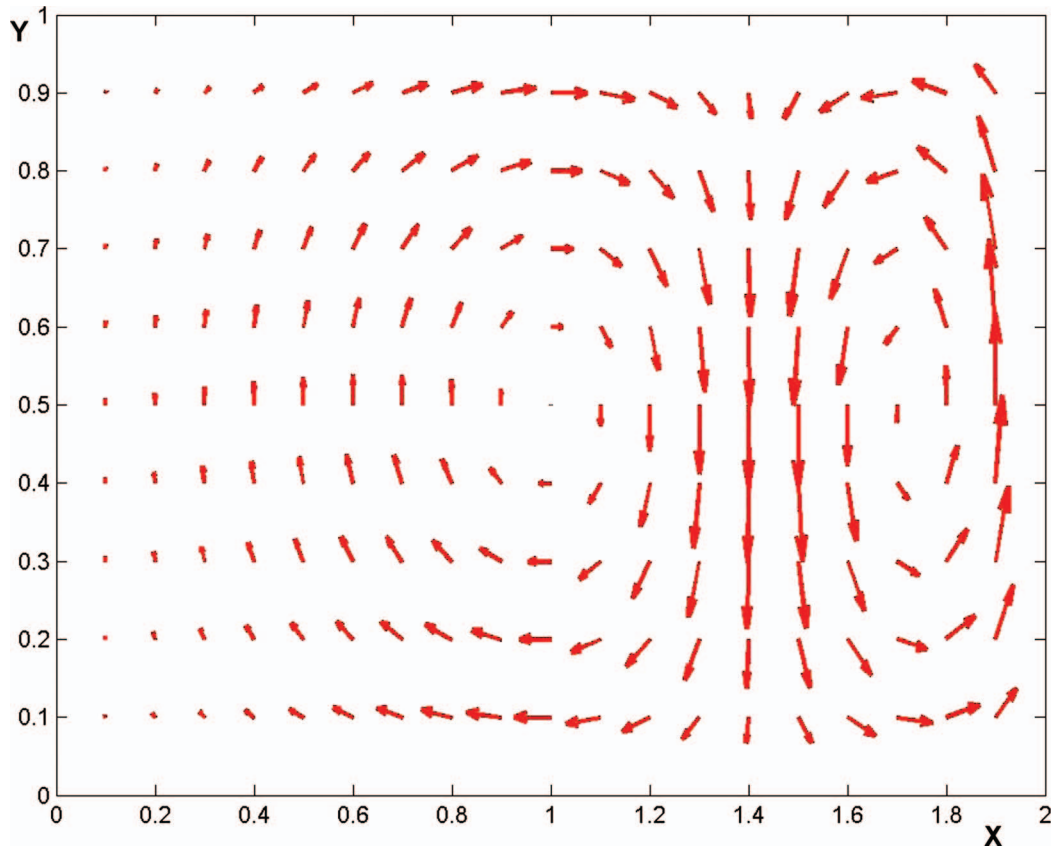


FIG. 1. The velocity field used for this model shown over the domain, \mathcal{D} , for a time when one of the gyres is near its maximal displacement from the centerline.

range chosen for the period will be explained in Sections III B and V C. If $\epsilon \geq 0.5$ the flow can bifurcate into more than two gyres. We fix $A = 0.1$. Hence, the parameter space is denoted explicitly by $\mathcal{P} = \{(T, \epsilon) \in \mathbb{R}^2 \mid 1 \leq T \leq 20, 0 \leq \epsilon \leq 0.5\}$. Figure 1 illustrates the velocity field.

III. EULERIAN INDICATORS FOR TWO-DIMENSIONAL, CONTINUOUSLY TIME VARYING VELOCITY FIELDS

In this section we will develop the EIs for two-dimensional, continuously time varying velocity fields. However, we will begin by establishing some general notation. The flow will be defined on a general two-dimensional domain, denoted \mathcal{D} . For the double-gyre model that we consider

$$\mathcal{D} = \{(x, y) \in \mathbb{R}^2 \mid 0 \leq x \leq 2, 0 \leq y \leq 1\}. \quad (5)$$

The flow will depend on parameters, and we will denote the space of parameters by \mathcal{P} , and a particular point in this parameter space by μ . For the double-gyre model

$$\mathcal{P} = \{(T, \epsilon) \in \mathbb{R}^2 \mid 1 \leq T \leq 20, 0 \leq \epsilon \leq 0.5\}. \quad (6)$$

The flow will be time dependent, and defined over a time interval denoted $\mathcal{I} \equiv [0, t_L]$, where t_L will be defined in Sec. III A 1.

The velocity field is denoted by

$$\begin{aligned} \dot{x} &= v_x(x, y, t; \mu), \\ \dot{y} &= v_y(x, y, t; \mu), \quad (x, y) \in \mathcal{D}, t \in \mathcal{I}, \mu \in \mathcal{P} \end{aligned} \quad (7)$$

or, in vector form

$$\dot{\mathbf{r}} = \mathbf{v}(\mathbf{r}, t; \mu), \quad (8)$$

where $\mathbf{r} \equiv (x, y)$, $\mathbf{v}(\mathbf{r}, t; \mu) \equiv (v_x(x, y, t; \mu), v_y(x, y, t; \mu))$.

We will need to perform averages of certain functions over the flow domain, parameter domain, and the time interval. For a general function $\mathbf{v}(\mathbf{r}, t; \mu)$ these averages are denoted by

$$\langle \mathbf{v}(\mathbf{r}, t; \mu) \rangle_{\mathbf{r}} \equiv \frac{1}{\int_{\mathcal{D}} d\mathbf{r}} \int_{\mathcal{D}} \mathbf{v}(\mathbf{r}, t; \mu) d\mathbf{r}, \quad (9)$$

$$\langle \mathbf{v}(\mathbf{r}, t; \mu) \rangle_{\mu} \equiv \frac{1}{\int_{\mathcal{P}} d\mu} \int_{\mathcal{P}} \mathbf{v}(\mathbf{r}, t; \mu) d\mu, \quad (10)$$

$$\langle \mathbf{v}(\mathbf{r}, t; \mu) \rangle_t \equiv \frac{1}{t'} \int_0^{t'} \mathbf{v}(\mathbf{r}, t; \mu) dt, \quad (11)$$

where $\int_{\mathcal{D}} d\mathbf{r}$ is an abbreviated notation for $\int_{\mathcal{D}} dx dy$. A specific choice for t' will be made later.

A. An Eulerian indicator for quantifying “streamline crossing” for two-dimensional continuously time-dependent flows

In this section we construct the EI that quantifies the notion of “streamline crossing” for two-dimensional continuously time-dependent flows. We begin by providing motivation for the construction.

1. Motivation

We develop our motivation by first recalling how streamline crossing is quantified for two-dimensional flows “blinking in time,” i.e., the flow periodically alternates between two distinct steady flows, in time. *Our discussion below concerns a fixed location in space.* We suppose that the first (steady) velocity field acts for a time t_1 and the second (steady) velocity field acts for a time t_2 . At a fixed location in space the first velocity vector makes an angle θ_1 with respect to the positive horizontal axis and the second velocity vector makes an angle θ_2 with respect to the positive horizontal axis, as illustrated in Figure 2(a). Streamline crossing, at this particular point in space, would occur if $\theta_1 \neq \theta_2$. Actually, it is a bit more complicated than this. In specifying streamline crossing we are not interested in the direction of flow—only that the streamlines cross. For this reason the direction of the arrows in Figure 2(a) are not important, and this issue does play a role in defining analytical formulae that quantify streamline crossing. Details for the blinking case can be found in Ref. 13.

Next, we turn to motivating the measure of streamline crossing for continuously time-dependent flows at a fixed point in space. First, note Figure 2(b) where, at the chosen point in space, we show the angle of the velocity vector (with respect to the positive horizontal axis) as a function of time.

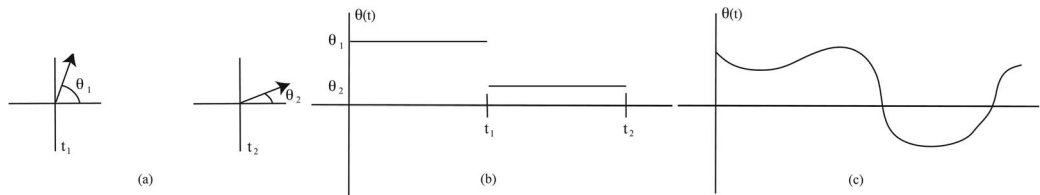


FIG. 2. Panels: (a) The angle that the velocity vector makes (with respect to the positive horizontal axis) for a blinking flow shown at a fixed location in space at two different times. (b) The angle that the velocity vector makes (with respect to the positive horizontal axis) for a blinking flow shown at a fixed location in space as a function of time. (c) The angle of the velocity vector (with respect to the positive horizontal axis), at a fixed location in space, for a continuously time varying velocity field.

If we are considering a velocity vector that varies continuously in time, then at the chosen point in space we would expect the angle of the velocity vector (with respect to the positive horizontal axis) to behave as in Figure 2(c). In this case, in analogy with the blinking flow case, a measure of streamline crossing (at the chosen point in space) is taken to be the standard deviation of the angle *over the time interval of interest* with respect to the mean value of the angle, and this is described by the square root of the variance of the angle. Clearly, this quantity would be zero for a steady two-dimensional flow, for which there is no streamline crossing. With this as motivation, we now develop this notion quantitatively.

2. Construction of the Eulerian indicator

In this section we derive our measure of “streamline crossing.” At a point $\mathbf{r} = (x, y)$ in the flow the angle that the velocity vector makes with respect to the positive horizontal (x) axis is given by

$$\theta(\mathbf{r}, t; \mu) = \text{atan} \left(\frac{v_y(x, y, t; \mu)}{v_x(x, y, t; \mu)} \right). \quad (12)$$

Then the mean angle at the point $\mathbf{r} = (x, y)$ over the time interval $[0, t_E]$ is defined as

$$\langle \theta(\mathbf{r}; \mu) \rangle_t \equiv \frac{1}{t_E} \int_0^{t_E} \theta(\mathbf{r}, t; \mu) dt. \quad (13)$$

The choice made for t_E will be discussed shortly, but for now we note that $t_E \ll t_L = 100$.

The essential quantity for computing the variance of $\theta(\mathbf{r}, t; \mu)$ is $\theta(\mathbf{r}, t; \mu) - \langle \theta(\mathbf{r}; \mu) \rangle_t$. Recall in the motivation at the beginning of this section we stated that in quantifying “streamline crossing” directionality of the velocity field was not important. Moreover, we will take the “smallest” angle between $\langle \theta(\mathbf{r}; \mu) \rangle_t$ and $\theta(\mathbf{r}, t; \mu)$. These two requirements are achieved in two steps. First, we insure that $\theta(\mathbf{r}, t; \mu) - \langle \theta(\mathbf{r}; \mu) \rangle_t$ is between $-\pi/2$ and $\pi/2$

$$\begin{aligned} \widehat{\theta}(\mathbf{r}, t; \mu) - \langle \theta(\mathbf{r}; \mu) \rangle_t = \\ \begin{cases} \theta(\mathbf{r}, t; \mu) - \langle \theta(\mathbf{r}; \mu) \rangle_t & \text{if } -\pi/2 < \theta(\mathbf{r}, t; \mu) - \langle \theta(\mathbf{r}; \mu) \rangle_t \leq \pi/2 \\ \pi - (\theta(\mathbf{r}, t; \mu) - \langle \theta(\mathbf{r}; \mu) \rangle_t) & \text{if } +\pi/2 < \theta(\mathbf{r}, t; \mu) - \langle \theta(\mathbf{r}; \mu) \rangle_t \leq \pi \\ -\pi - (\theta(\mathbf{r}, t; \mu) - \langle \theta(\mathbf{r}; \mu) \rangle_t) & \text{if } -\pi < \theta(\mathbf{r}, t; \mu) - \langle \theta(\mathbf{r}; \mu) \rangle_t \leq -\pi/2 \end{cases} \end{aligned}$$

This expression is used to compute the variance of the angles at the point $\mathbf{r} = (x, y)$ in the flow over the time interval $[0, t_E]$,

$$\mathcal{V}_\theta(\mathbf{r}; \mu, t_E) \equiv \frac{1}{t_E} \int_0^{t_E} (\widehat{\theta}(\mathbf{r}, t; \mu) - \langle \theta(\mathbf{r}; \mu) \rangle_t)^2 dt. \quad (14)$$

The square root of $\mathcal{V}_\theta(\mathbf{r}; \mu, t_E)$ has the units of an angle. However, it is not quite the measure of averaged transversality of the velocity vectors over the time interval $[0, t_E]$ that we seek. The reason for this is that the integrand in Eq. (14) is squared so that $0 \leq \widehat{\theta}(\mathbf{r}, t; \mu) - \langle \theta(\mathbf{r}; \mu) \rangle_t \leq \pi/2$ contributes exactly the same as $-\pi/2 \leq \widehat{\theta}(\mathbf{r}, t; \mu) - \langle \theta(\mathbf{r}; \mu) \rangle_t \leq 0$. To see the problem that can arise consider the two angles $\widehat{\theta}(\mathbf{r}, t; \mu) - \langle \theta(\mathbf{r}; \mu) \rangle_t = \pi/2$ and $\widehat{\theta}(\mathbf{r}, t; \mu) - \langle \theta(\mathbf{r}; \mu) \rangle_t = -\pi/2$. These angles correspond to velocity vectors along the same line, but in opposite directions. This is a situation that is not indicative of “streamline crossing,” yet these two angles contribute equally to Eq. (14). Alternatively, the two angles $\widehat{\theta}(\mathbf{r}, t; \mu) - \langle \theta(\mathbf{r}; \mu) \rangle_t = \pi/4$ and $\widehat{\theta}(\mathbf{r}, t; \mu) - \langle \theta(\mathbf{r}; \mu) \rangle_t = -\pi/4$ correspond to two velocity vectors that are perpendicular, which should be the maximal indicator of streamline crossing. With this as motivation, we have

$$\theta_{RMS}(\mathbf{r}; \mu, t_E) = \sqrt{\mathcal{V}_\theta(\mathbf{r}; \mu, t_E)} \quad (15)$$

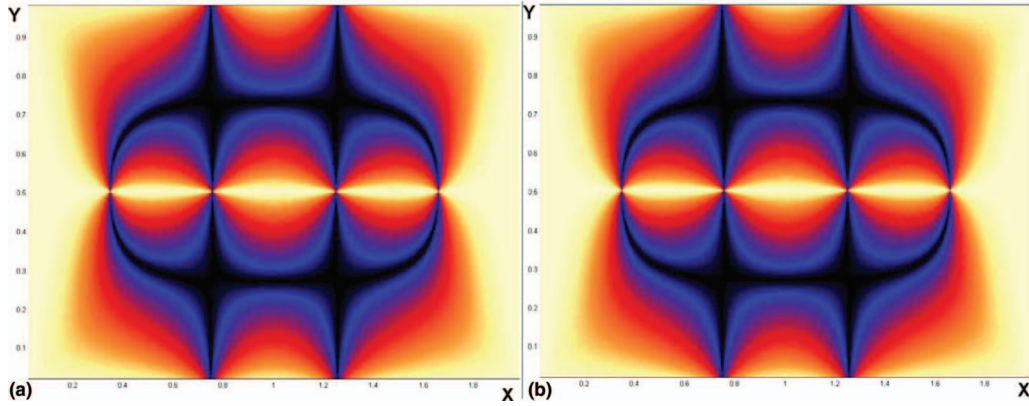


FIG. 3. Transversality for the square wave time dependence shown over the spatial domain, \mathcal{D} : (a) the continuous time definition of transversality, $\alpha_c(\mathbf{r}; \mu, t_E)$ and (b) the discrete definition of transversality, $\alpha(\mathbf{r}; \mu, t_E)$. For both cases $T = 20$ and $\epsilon = 0.27$.

and we take the following as our measure of “transversely intersecting streamlines” (or, more concisely, “transversality”) or “streamline crossing”: at a point $\mathbf{r} = (x, y)$,

$$\alpha_c(\mathbf{r}; \mu, t_E) = \begin{cases} 2\theta_{RMS}(\mathbf{r}; \mu, t_E) & \text{if } 0 < \theta_{RMS}(\mathbf{r}; \mu, t_E) \leq \pi/4 \\ 2(\pi/2 - \theta_{RMS}(\mathbf{r}; \mu, t_E)) & \text{if } \pi/4 < \theta_{RMS}(\mathbf{r}; \mu, t_E) \leq \pi/2 \end{cases}. \quad (16)$$

The average of $\alpha_c(\mathbf{r}; \mu, t_E)$ over the flow domain is denoted by

$$\bar{\alpha}_c(\mu, t_E) = \langle \alpha_c(\mathbf{r}; \mu, t_E) \rangle_{\mathbf{r}} = \frac{\int_{\mathcal{D}} \alpha_c(\mathbf{r}; \mu, t_E) d\mathbf{r}}{\int_{\mathcal{D}} d\mathbf{r}}. \quad (17)$$

As should be the case following the discussion at the beginning of this section, we show that our new continuous time definition of transversality gives the same result as the definition of transversality given in Refs. 13, 15, and 16 for blinking flows. The square wave time dependence is a blinking flow. Figures 3(a) and 3(b) show a comparison of the transversality EI for the square wave time dependence with a value of $T = 20$ and $\epsilon = 0.27$ for the continuous time definition, $\alpha_c(\mathbf{r}; \mu, t_E)$, compared to the discrete definition of $\alpha(\mathbf{r}; \mu, t_E)$, defined in Refs. 13, 15, and 16. Transversality is shown in both cases as a contour map across the spatial domain. The results are identical for both cases.

B. A measure of the relative rate of (temporal) change of a velocity field

In this section we introduce a metric to measure and quantify the temporal rate of change of the velocity field. We begin by defining the quantity, Eq. (18), that is a measure of the relative change of the velocity vector at a point, \mathbf{r} , between two points in time separated by Δt with certain properties

$$\Delta w(\mathbf{r}, t; \mu) = \frac{\|\mathbf{v}(\mathbf{r}, t + \Delta t; \mu) - \mathbf{v}(\mathbf{r}, t; \mu)\|}{\|\mathbf{v}(\mathbf{r}, t + \Delta t; \mu)\| + \|\mathbf{v}(\mathbf{r}, t; \mu)\|} = \begin{cases} 0 & \text{if } \mathbf{v}(\mathbf{r}, t + \Delta t; \mu) = \mathbf{v}(\mathbf{r}, t; \mu) \\ 1 & \text{if } \mathbf{v}(\mathbf{r}, t + \Delta t; \mu) = -\mathbf{v}(\mathbf{r}, t; \mu) \\ 1 & \text{if } \mathbf{v}(\mathbf{r}, t + \Delta t; \mu) = 0 \\ 1 & \text{if } \mathbf{v}(\mathbf{r}, t; \mu) = 0 \end{cases}. \quad (18)$$

By construction $\Delta w(\mathbf{r}, t; \mu)$ has the following properties.

- It is “scale independent” in the sense that it measures the relative rate of change of a velocity vector in a manner that is independent of the amplitude of the time variation or the magnitude of the vector.

- It measures both a change in magnitude and a change in direction of the velocity vector at the point \mathbf{r} .
- It is nonnegative, so that when it is integrated with respect to time it measures a “total change” over the time interval of integration.

Taking the limit as Δt approaches 0, we define the differential,

$$dw(\mathbf{r}, t; \mu) = \lim_{\Delta t \rightarrow 0} \Delta w(\mathbf{r}, t, \Delta t; \mu). \quad (19)$$

By integrating Eq. (19) over an interval of time, $[0, t_E]$ we obtain a relative rate of change over this time interval for each position in the spatial domain

$$\tilde{w}(\mathbf{r}; \mu) = \frac{1}{t_E} \int_0^{t_E} dw(\mathbf{r}, t; \mu), \quad (20)$$

which we refer to as the RROC. The time, t_E , is chosen to be an integral multiple of T , mT , where m has the property that it is the largest integer such that $mT \leq 20$, $(m+1)T > 20$, making the fact that the right-hand side of Eq. (20) behaves as $\frac{1}{T}$ for the range $1 \leq T \leq 20$ is evident. This behavior is further explored in Appendix A.

Finally, averaging Eq. (20) over the spatial domain gives the net relative rate of change for a velocity field over the time interval $[0, t_E]$. The EI given in Eq. (21), denoted $\zeta(\mu)$, is then a measure of the relative rate of change for the entire velocity field. The interpretation of ζ will be discussed in Sec. V,

$$\zeta(\mu) \equiv \frac{1}{\int_{\mathcal{D}} d\mathbf{r}} \int_{\mathcal{D}} \tilde{w}(\mathbf{r}; \mu) d\mathbf{r}. \quad (21)$$

C. An Eulerian indicator for quantifying mobility

In this section we construct an EI, “mobility” (η) having the following properties.

- Mobility quantifies the percentage of the domain where particles are transported away from their initial location.
- Mobility is sensitive to time scales in the sense that it is dependent upon the product of the characteristic time of the fluid flow and the rate at which the velocity field is changing (the RROC).
- The use of a threshold velocity has two important implications for mobility. One is that mobility is insensitive to the extent to which the velocity threshold is exceeded (cf. (30)). The other is that no contribution to mobility is made by regions of the flow that are below the velocity threshold (cf. (29)).
- Mobility is reduced in value by regions of the flow where the velocity field is uniformly low in value, or where the velocity field changes rapidly in time, resulting in cancellation of the velocity. Each of these situations is quantified in relation to the threshold velocity (cf. (25) and (29)).
- Mobility is increased in value by regions of the flow where the velocity field is uniformly high, or where the velocity vectors are sufficiently aligned over time. Each of these situations is quantified in relation to the threshold velocity (cf. (25) and (29)).

The characteristic time scale, T_c , that we will use is particular to the geometry of the flow and is discussed in some detail in Appendix B. Essentially, it is the eddy turnover time associated with a typical gyre.

To begin with, we note the following formula for the displacement (i.e., transport) of fluid particles

$$|\mathbf{r}(t_E) - \mathbf{r}(0)| = \left| \int_0^{t_E} \mathbf{v}(\mathbf{r}, t; \mu) dt \right| \leq \int_0^{t_E} |\mathbf{v}(\mathbf{r}, t; \mu)| dt. \quad (22)$$

The two terms on the right of this formula involving different types of the integral of the velocity field over time will serve as our motivation for characterizing “fast” and “slow” changing flows.

For “fast” changing flows, we consider the magnitude of the integrated velocity vectors at a point in the domain

$$v_{\text{fast}}(\mathbf{r}; \mu) \equiv \left| \int_0^{t_E} \mathbf{v}(\mathbf{r}, t; \mu) dt \right|. \quad (23)$$

The rationale behind taking the magnitude of the integral is that for “fast” changing flows, the velocity vectors, at a point, have the possibility to exhibit cancelation over time.

For “slow” changing flows, we consider the integral of the magnitude of the velocity field at a point in the domain

$$v_{\text{slow}}(\mathbf{r}; \mu) \equiv \int_0^{t_E} |\mathbf{v}(\mathbf{r}, t; \mu)| dt. \quad (24)$$

The rationale behind taking the integral of the magnitude for “slow” changing flows is that velocity fields which vary slowly effect transport of particles away from a region in such a way that cancelation of velocity vectors over time does not occur.

The definition of “fast” and “slow” depends upon the time scale under consideration, and they are given meaning through the characteristic time scale, T_c , and the RROC, as follows:

$$v_{\text{sum}}(\mathbf{r}; \mu) \equiv (1 - e^{-\tilde{w}(\mathbf{r}; \mu)T_c}) v_{\text{fast}}(\mathbf{r}; \mu) + (e^{-\tilde{w}(\mathbf{r}; \mu)T_c}) v_{\text{slow}}(\mathbf{r}; \mu), \quad (25)$$

where $\tilde{w}(\mathbf{r}; \mu)$ is the RROC and T_c is the characteristic time scale. The integrated velocity magnitude, $v_{\text{sum}}(\mathbf{r}; \mu)$, is then the weighted magnitude which is sensitive to the natural time scale of the flow as well as the rate of change of the velocity field. For large values of $\tilde{w}(\mathbf{r}; \mu)T_c$, the main contribution to $v_{\text{sum}}(\mathbf{r}; \mu)$ is from $v_{\text{fast}}(\mathbf{r}; \mu)$ and for small values of $\tilde{w}(\mathbf{r}; \mu)T_c$, the main contribution to $v_{\text{sum}}(\mathbf{r}; \mu)$ is from $v_{\text{slow}}(\mathbf{r}; \mu)$. It follows from Eq. (22) that $v_{\text{sum}}(\mathbf{r}; \mu)$ is larger when $v_{\text{slow}}(\mathbf{r}; \mu)$ makes the dominant contribution to Eq. (25).

In our previous study,¹⁶ a threshold value for $v_{\text{sum}}(\mathbf{r}; \mu)$ was determined as follows. The spatial average of $v_{\text{sum}}(\mathbf{r}; \mu)$ is given by

$$\overline{v_{\text{sum}}(\mu)} = \langle v_{\text{sum}}(\mathbf{r}; \mu) \rangle_{\mathbf{r}} \equiv \frac{\int_{\mathcal{D}} v_{\text{sum}}(\mathbf{r}; \mu) d\mathbf{r}}{\int_{\mathcal{D}} d\mathbf{r}}. \quad (26)$$

Averaging this quantity over the parameter space gives

$$\widetilde{v_{\text{sum}}} = \langle \overline{v_{\text{sum}}(\mu)} \rangle_{\mu} \equiv \frac{\int_{\mathcal{P}} \overline{v_{\text{sum}}(\mu)} d\mu}{\int_{\mathcal{P}} d\mu}. \quad (27)$$

The resulting value, $\widetilde{v_{\text{sum}}}$, we take as the *threshold value*

$$v_{\text{thresh}} = \widetilde{v_{\text{sum}}}. \quad (28)$$

This is the fundamental quantity for determining which values of the weighted summed velocity vector are considered “high” versus “low.” In particular, we consider the points in the domain having the property that $v_{\text{sum}}(\mathbf{r}; \mu) \geq v_{\text{thresh}}$ – the “mobile” points. These points are given by

$$\mathcal{M}(\mu) = \{\mathbf{r} \in \mathcal{D} \mid v_{\text{sum}}(\mathbf{r}; \mu) \geq v_{\text{thresh}}\} \quad (29)$$

The indicator function that assigns the value 1 to points in $\mathcal{M}(\mu)$ and 0 to points in the flow domain that are not in $\mathcal{M}(\mu)$ is given by

$$\mathbb{I}_{\mathcal{M}(\mu)}(\mathbf{r}) \equiv \begin{cases} 1 & \text{if } \mathbf{r} \in \mathcal{M}(\mu) \\ 0 & \text{if } \mathbf{r} \in \mathcal{D} \setminus \mathcal{M}(\mu) \end{cases}. \quad (30)$$

Finally, the mobility is defined as

$$\eta(\mu) \equiv \frac{\int_{\mathcal{D}} \mathbb{I}_{\mathcal{M}(\mu)}(\mathbf{r}) d\mathbf{r}}{\int_{\mathcal{D}} d\mathbf{r}}. \quad (31)$$

Hence, the mobility is a measure of the percentage of the region of points in the domain, \mathcal{D} , where $v_{\text{sum}}(\mathbf{r}, \mu)$ is greater than the threshold. A high value of mobility, $\eta(\mu)$, corresponds to a flow whose

spatial domain, \mathcal{D} , has a high percentage of good transport regions and a low percentage of stagnant regions, regions with little net displacement. We note that the quantities and methodology for computing mobility in blinking flows, as first introduced in Ref. 16, are the same as for continuously time varying flows that we have just described. The only difference is in the form of the term Eq. (25).

The procedure for computing mobility described above is applied to a particular velocity field. However, in this paper we are comparing the mixing properties of five different time dependencies. Effectively, this represents five different models. In comparing mobility for the five different time dependencies we want it to be defined in such a way that the differences in the mobility for the five models is directly related to the different time dependencies. Now recall from Eq. (29) that the mobile points are defined in terms of a threshold velocity for a given velocity field. In order to use mobility to compare the different time dependencies we wish to have a threshold velocity that is *the same* for each model in such a way that the difference in mobility can be directly ascribed to the difference in time dependence. To this end, we compute a threshold velocity that is common to each model, and takes into account the geometric features of the flow common to each model, as follows. The threshold velocity is obtained by computing the magnitude of the spatial average of the *steady* double gyre over the region $0.5 \leq x \leq 1.5$, $0 \leq y \leq 1$. The threshold velocity determined in this way is $v_{\text{thresh}} = 0.183$. The mobility is then computed for each of the five different time-dependent models using Eqs. (25) and (29)–(31) exactly as described above. However, the common threshold velocity, $v_{\text{thresh}} = 0.183$, is used in Eq. (29) for each of the five different time-dependent models in order to determine the “mobile points” for each model.

IV. DEGREE OF MIXING OF TWO FLUIDS: VARIANCE OF CONCENTRATION

In order to demonstrate the effectiveness of the EIs for predicting different features of (Lagrangian) mixing we will need a particle trajectory based diagnostic that quantifies the extent of which two fluids are mixed. There is significant literature on quantifying mixing, see, e.g., Ref. 18. In this paper we will use the normalized variance of concentration as originally described by Danckwerts, see Refs. 3 and 4. The numerical implementation of the method is standard. Our approach is described in Refs. 13, 15, and 16. Below we give a brief outline of the elements of the method that are important for interpreting our results.

Consider a mixture of two separate fluids, which we designate red and blue. The relative concentration of red fluid in some subdomain at some later time is given by

$$c = \frac{\#red}{(\#red + \#blue)}, \quad (32)$$

where $\#red$ and $\#blue$ denote the number of red particles and the number of blue particles, respectively, in this area of interest at that instant.

We divide the domain into smaller regions, or bins, and, at each time, the local concentration in each bin is calculated, as described in Eq. (32). Mixing is quantified by computing the difference between the local concentration in each bin and the concentration over the entire domain (which does not change in time), squaring the difference, and then averaging over all the bins. In this way, we obtain the variance of concentration as a function of time, $\mathcal{V}(t)$,

$$\mathcal{V}(t) = \frac{1}{N_{bins}} \sum_{i=1}^{N_{bins}} (c_i(\mathbf{r}_i, t) - c_{avg})^2. \quad (33)$$

A total of 800 bins are used forming a 40×20 grid in the 2×1 rectangular domain. This division of the domain allows a local concentration to be computed in each bin at a given time, which we denote by $c_i(\mathbf{r}_i, t)$, where i is the index labeling a bin and \mathbf{r}_i denotes the position of the bin. Since the concentration of red over the entire domain does not change in time, the average concentration over the entire domain, denoted c_{avg} , is constant in time and equal to 50%. The variance is a measure of how different each local concentration is relative to the average.

For this study, the fluids were initially separated in a left-right orientation. From an initially unmixed state, the variance of concentration falls to a lower value over time, indicating mixing has occurred. When the value of the variance of concentration reaches zero, each subdomain is fully mixed.

The general behavior observed for the decay of variance of concentration is exponential. Each simulation was performed to a final time of $t_L = 100$. This time was found to be long enough that asymptotic behavior can be observed. In a large fraction of the simulations, the fluid would appear to reach a constant value for the variance of concentration, suggesting that it will never mix better than a certain amount. As a result, the time dependence of $\mathcal{V}(t)$ is fitted to the expression

$$\mathcal{V}(t) = (\mathcal{V}(0) - \text{bias})e^{-t/\tau} + \text{bias}, \quad (34)$$

where the parameter τ is the time constant for the decay of $\mathcal{V}(t)$ and *bias* is the long-time behavior of $\mathcal{V}(t)$. The bias term accounts for the fact that some flow configurations never mix well. Flows that exhibit large “islands,” i.e., regions that do not mix with their surroundings, are good examples of high-bias configurations. The parameters τ and *bias* provide an indication of the quality of mixing. The decay is fast whenever τ is low. If, however, the bias term is high, a low value of τ can give a false impression of fast mixing. In this case, the variance of concentration quickly decays from a high initial value, $\mathcal{V}(0)$, down to a high bias value. Such mixers quickly approach their asymptotic performance, but this performance is poor. Low τ is therefore not sufficient to indicate good mixing. A low value of *bias* indicates good mixing at very long times, but if coupled with a high value of τ , the mixing is slow. Small values of both τ and *bias* give the best mixing performance.

V. RESULTS: QUALITY OF MIXING, EULERIAN INDICATORS, AND COMPUTATIONAL EFFICIENCY

A. Quality of mixing results

Figures 4 and 5 show the Lagrangian results for these simulations, which characterize the quality of mixing for each time-dependent function studied. Figure 4 shows the variance of concentration as a surface plot of variance. Figure 5 shows the tau-bias fit results. For comparison with EIs discussed in Secs V B and V C, the variance of concentration is shown in the parameter space with the period (T) along one axis and the amplitude (ϵ) along the other axis. The tau-bias figure is related to the time dependence of the variance of concentration. Previous studies have shown that the “best” mixers are the ones which mix fast (low tau values) as well as completely (low bias values). This suggests that configurations in the tau-bias plane which populate the lower left-hand corner are the best mixers, becoming relatively poorer as the values move away from this corner. As a subjective measure, the configurations considered were rank ordered based on their variance of concentration value at the final time of $t_L = 100$. The lowest 10% values were considered the “best,” followed by the next lowest 20% values, labeled “good,” then the next 20%, labeled “medium” followed by the remaining 50%, labeled “poor” mixers. The mixing configurations are represented in the tau-bias plane as colored dots, where the darkest (black) dots are the “best” mixers and the lightest (yellow) are the “poor” mixers. In order to present the surface of variance of concentration such that the best mixers were elevated, the normally low values associated with the variance of concentration were inverted for the surface plots. For more discussion of these technical issues, please see Refs. 15 and 16.

A summary of the results from Figure 4 leads to the following conclusions.

1. Generally, the larger the displacement (ϵ) of the gyres away from the centerline (i.e., asymmetric gyres) the greater the mixing.
2. The longer the period of the oscillation, the greater the mixing, for the finite time interval on which we have quantified the mixing.
3. Fast oscillations lead to poor or no mixing.
4. The plateau in the T - ϵ parameter space which indicates good mixing exists independent of the type of time dependence for $a(\omega t)$.

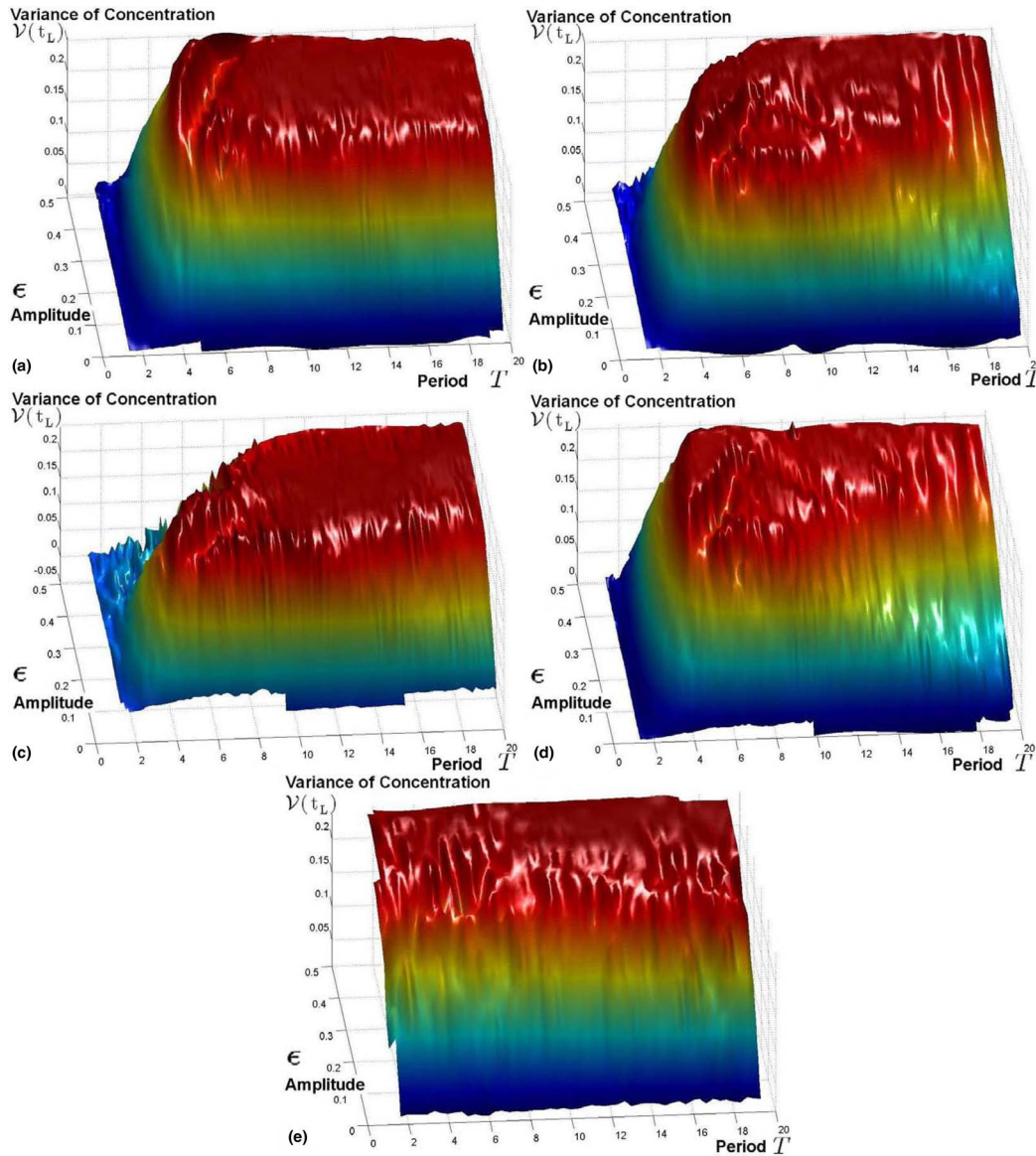


FIG. 4. Comparison of plots for all five time dependencies for the surface of variance of concentration, $\mathcal{V}(t_L)$ shown over the parameter space in each frame, \mathcal{P} ; (a) sawtooth, (b) sinusoid, (c) square wave, (d) triangle, and (e) noise.

Points one and two of these general conclusions lead to the large plateau seen for the parameter space of T - ϵ in each of the variance of concentration plots, *independent of the type of time dependence*. Point three is addressed in detail in Sec. III C. When $a(\omega t)$ oscillates too quickly, the velocity vector field can change direction so quickly that a particle does not have time to transport significantly across the domain, contributing to poor mixing.

B. Eulerian indicator results

Figures 6 through 9 show the results of the EI computations for the five time dependencies studied in this paper. The parameter space shown is of the period of oscillation, T , on one axis versus the strength of the time dependence, ϵ , on the other axis. Figure 6 shows the surface of the transversality, $\bar{\alpha}_c$. Figure 7 shows the spatially averaged RROC, denoted ζ . Figure 8 shows the surface of the mobility, η . Figure 9 shows a view from above of the surface of the product of

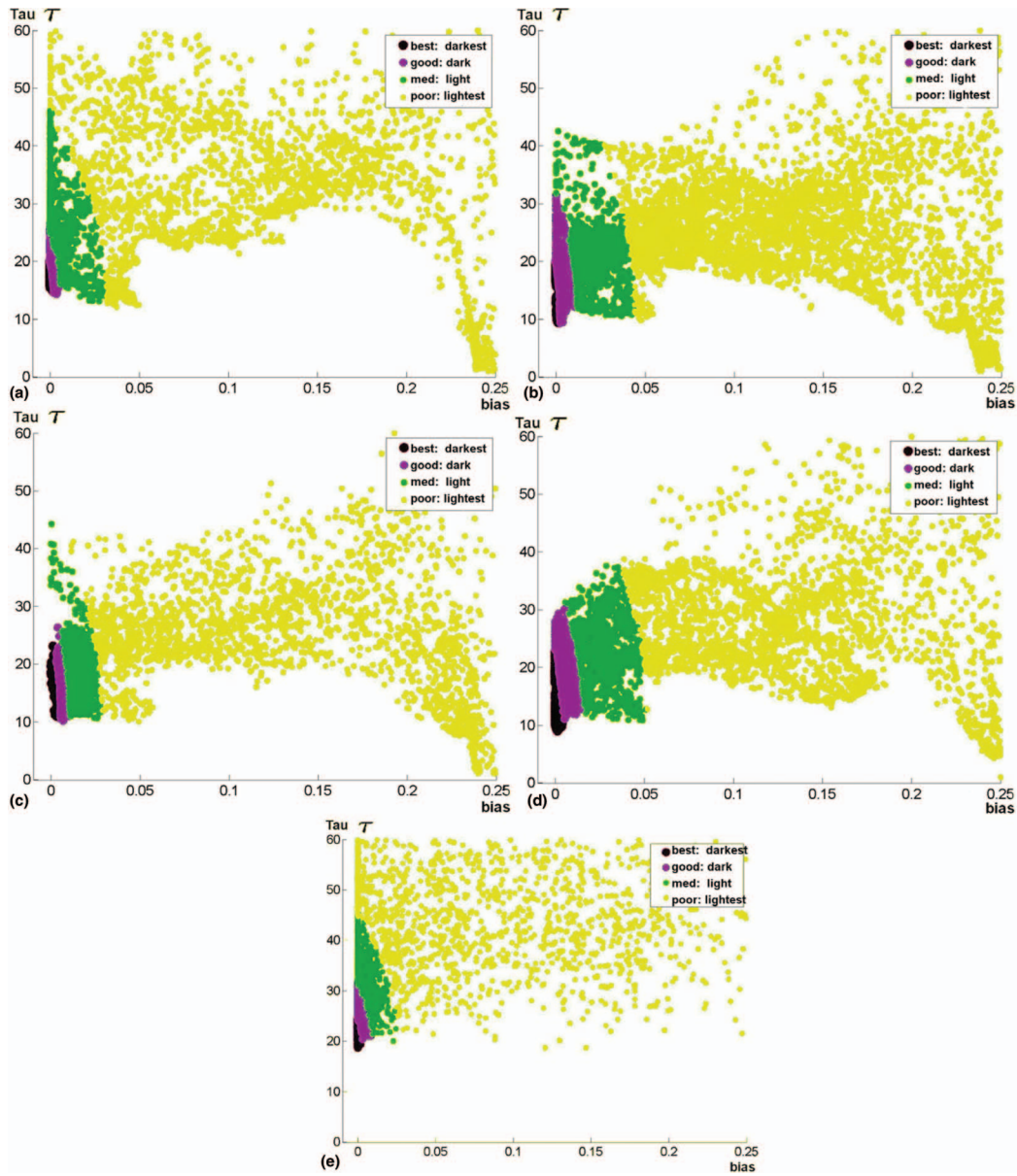


FIG. 5. Comparison of plots for all five time dependencies for the tau versus bias values; (a) sawtooth, (b) sinusoid, (c) square wave, (d) triangle, and (e) noise. The “best” mixers are the darkest, “good” mixers are dark, “medium” mixers are light, and “poor” mixers are the lightest colored dots.

transversality and mobility, $\bar{\alpha}_c \eta$ overlaid with the contours of the variance of concentration at a time $t_L = 100$. Within each figure, the five plots: (using transversality as an example) Figs. 6(a), 6(b), 6(c), 6(d), and 6(e), show the sawtooth, sinusoidal, square wave, triangle, and noisy time dependencies, respectively.

Figures 6(a)–6(e) show that the transversality, $\bar{\alpha}_c$, does not exhibit any dependence on the period, T . While calculating $\bar{\alpha}_c$, the statistical set used to measure the variance of the angles is over one full period, which will be true for any length of the period, explaining why no period dependence is observed. A longer period would simply have more angles contribute to the mean and variance, making the result more statistically significant, however, not changing the value of the mean angle. As the maximal displacement of the gyres away from the center, ϵ , increases, the variance of the angles used to calculate $\bar{\alpha}_c$ increase as well, explaining the rise of $\bar{\alpha}_c$ with increasing displacement.

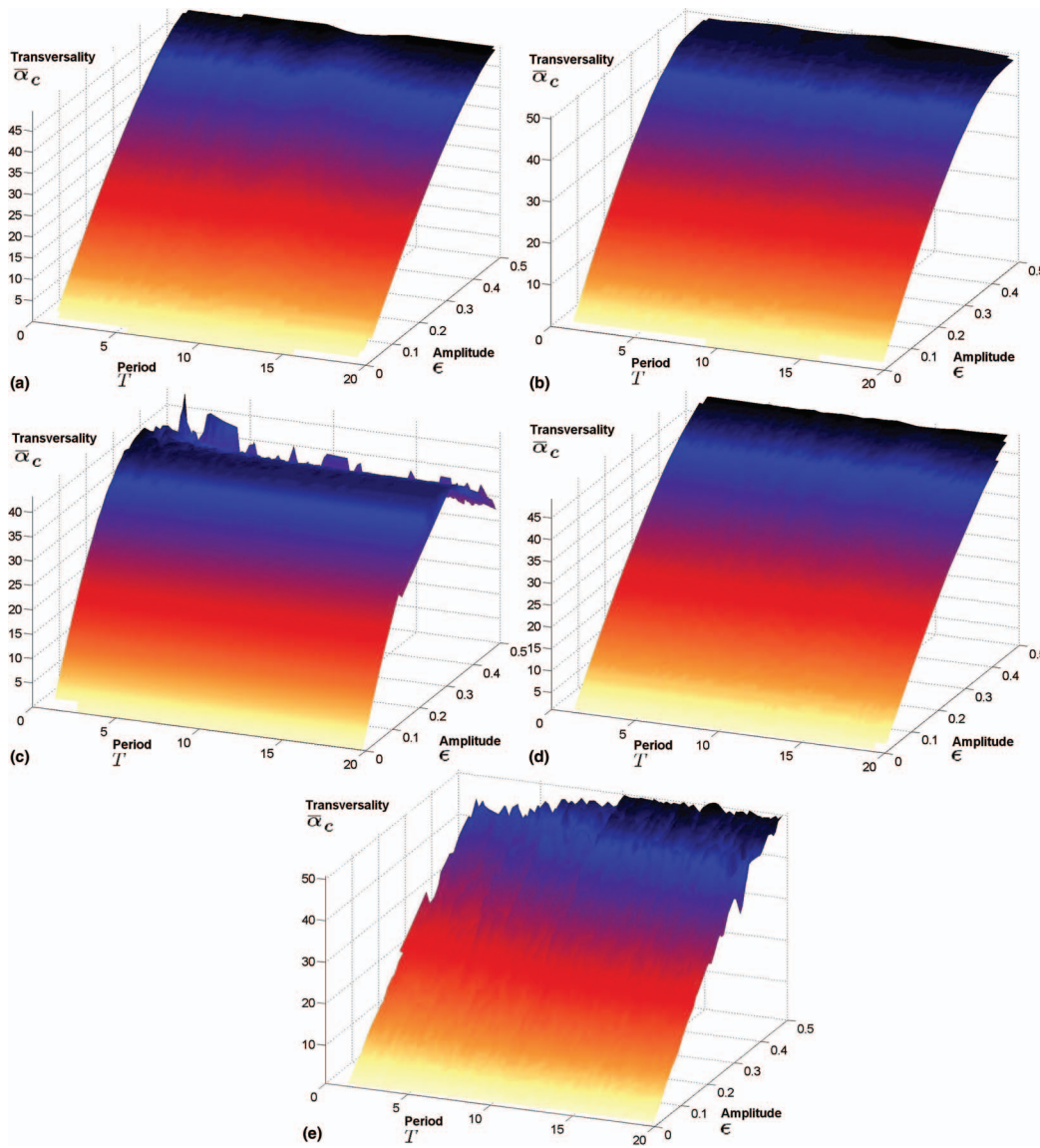


FIG. 6. Comparison of plots for all five time dependencies for the transversality, $\bar{\alpha}_c$, shown over the parameter space in each frame, \mathcal{P} ; (a) sawtooth, (b) sinusoid, (c) square wave, (d) triangle, and (e) noise.

Figures 7(a)–7(e) show the EI for the spatially averaged RROC, denoted ζ , over the domain, \mathcal{P} . For each time dependence studied, the effect across the parameter space is similar. Zeta, $\zeta(\mu)$, linearly increases as ϵ increases due to more of the domain, \mathcal{D} , engaged in a higher rate of change. Also, $\zeta(\mu)$, decreases as the period increases with a $\frac{1}{T}$ dependence.

Figures 8(a)–8(e) show the mobility over the parameter space. Mobility has the opposite dependence on ϵ compared to transversality. When the maximal displacement of the gyres is low (close to zero) the velocity field exhibits little oscillation and the velocity vectors remain aligned over the time interval of the simulation. In this case, transport is possible since the canceling effect of an oscillating vector field is not present, which may result in a high value for mobility. As ϵ increases, more locations in the domain may experience large changes in their velocity (both in direction and magnitude), and the possibility of velocity vectors canceling over a specified time interval may lead to some locations experiencing a much lower net velocity vector over this time interval. In this situation, the mobility value may decrease. The dependence of the mobility on the period can be understood as follows. From the discussion following Eq. (20), when the period, T , is short, the RROC

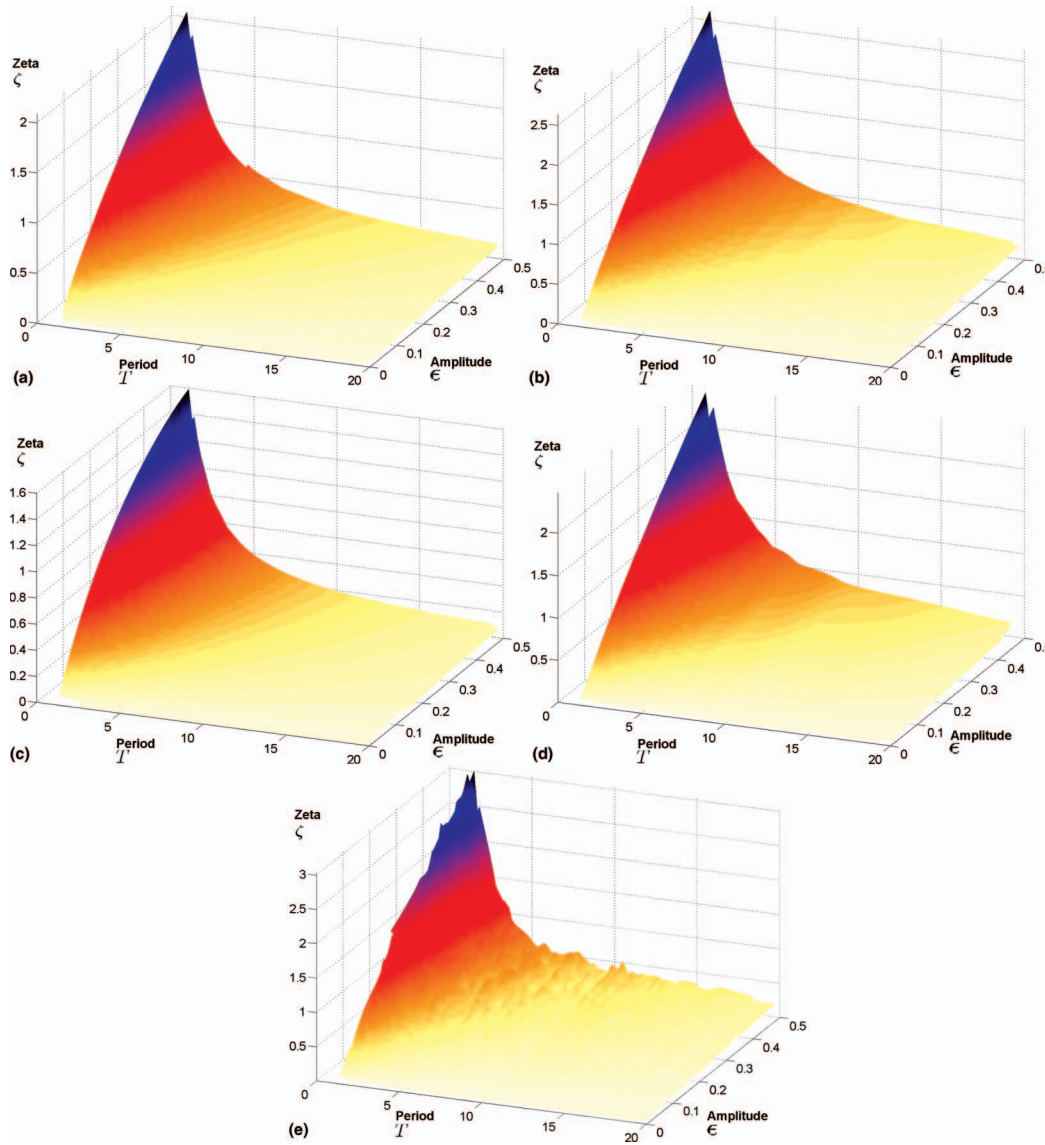


FIG. 7. Comparison of plots for all five time dependencies for ζ , shown over the parameter space in each frame, \mathcal{P} ; (a) sawtooth, (b) sinusoid, (c) square wave, (d) triangle, and (e) noise.

increases and when the period is long, the RROC decreases. Recalling the discussion following Eq. (25), as the RROC decreases $v_{\text{sum}}(\mathbf{r}; \mu)$ increases and as the RROC increases $v_{\text{sum}}(\mathbf{r}; \mu)$ decreases. This implies that in the former case there are more points in the domain contributing to the mobility than in the latter case (cf. (29) and (30)). In other words, when the period decreases, the mobility decreases and when the period increases, the mobility increases, and this is what is observed in Figures 8(a)–8(e).

Figures 9(a)–9(e) show the product of transversality and mobility as a surface. Due to the rising values of $\bar{\alpha}_c$ and the falling values of mobility, when the two EI quantities are multiplied, generally a parabolic surface is created along a medium value for the maximal displacement of the gyres, near $\epsilon = 0.25$ – 0.35 . Due to the dependence on the period for mobility, the region with low period and high ϵ tends to reach a minimal value for the product, $\bar{\alpha}_c \eta$. Contours of the variance of concentration have been overlaid with this surface to allow a comparison between the Lagrangian metric for mixing quality with the Eulerian prediction. Generally, the EIs predict the plateau of best mixing as shown in the upper values of the period and the highest values of ϵ . This shows that although not every feature

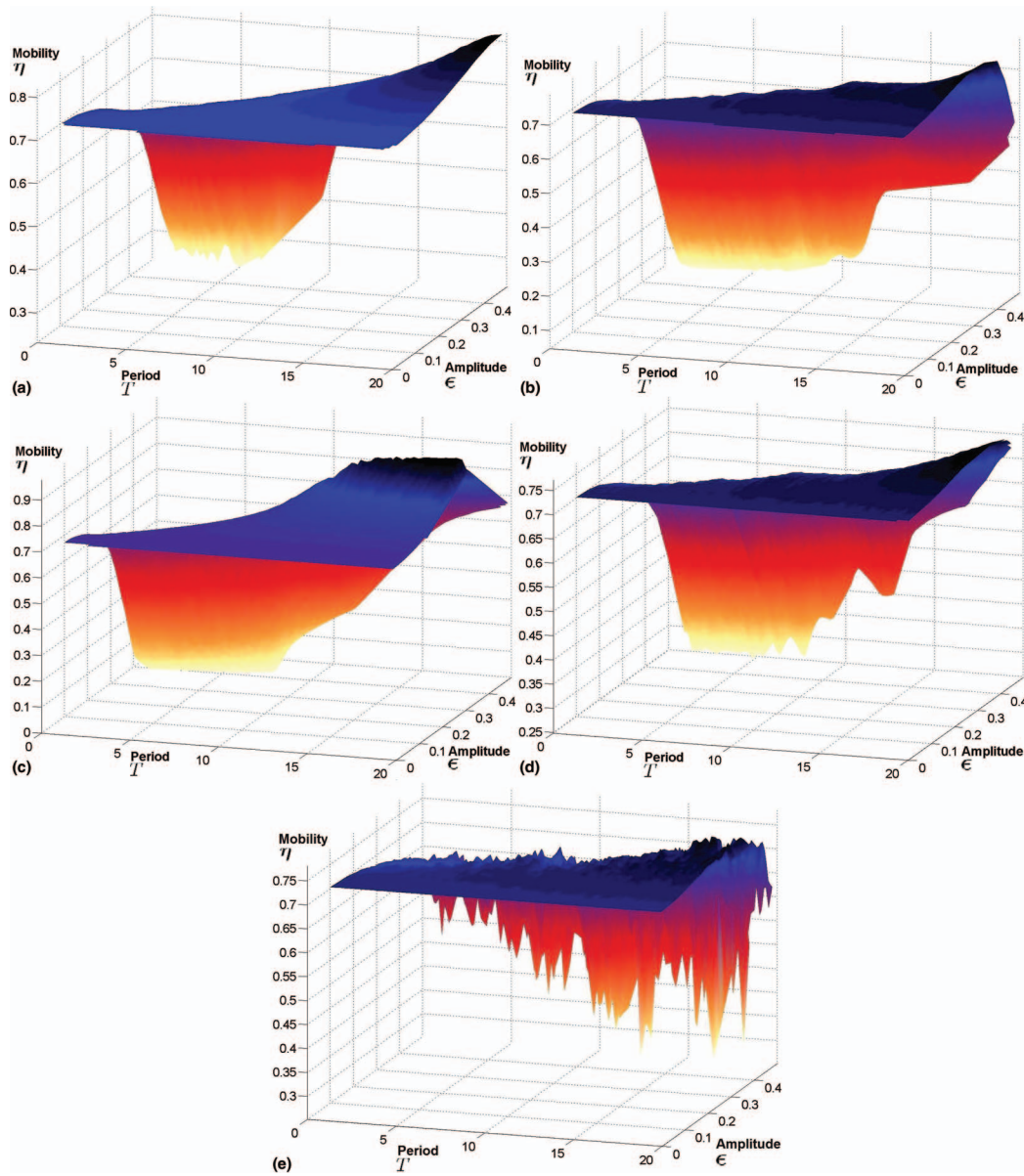


FIG. 8. Comparison of plots for all five time dependencies for the mobility, η , shown over the parameter space in each frame, \mathcal{P} ; (a) sawtooth, (b) sinusoid, (c) square wave, (d) triangle, and (e) noise.

of the mixing quality is captured by EIs, they do in general predict the regions in the parameter space studied that correspond to good mixing.

Similar to our results from a previous study of the 2D Lid-Driven model described in Ref. 16, the product of transversality and mobility (EI) was used to compare to the quality of mixing (Lagrangian) to validate whether EIs can predict good mixing. Figures 9(a)–9(e) show this comparison as a single graph, where the contours overlaid on the surface shown are the contours from the Lagrangian mixing quality, whereas the surface beneath is the product of transversality and mobility.

It is useful to point out here that our results show that transversality alone (i.e., “streamline crossing”) is not necessarily correlated with good mixing. This is not too surprising since, as we discussed at the beginning of this section, transversality does not exhibit a dependence on the period. Rather, it is the product of transversality with mobility (which does exhibit a period dependence) that best correlates with the quality of mixing, as shown by the decay of the concentration of variance.

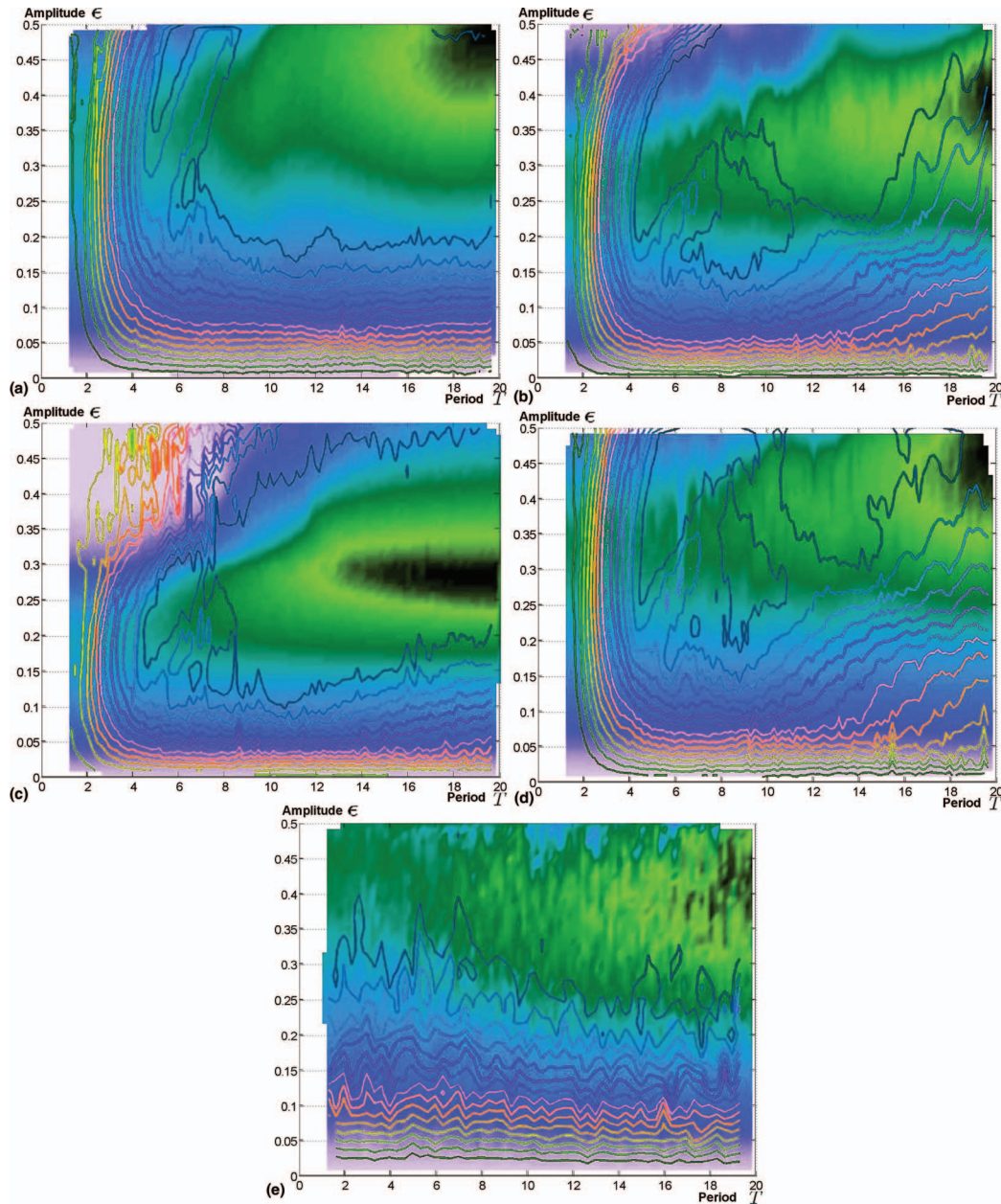


FIG. 9. Comparison of plots for all five time dependencies for the overlay of the product of transversality and mobility with the contours of the variance of concentration, $\bar{\alpha}_c \eta$ and $\mathcal{V}(t)$, shown over the parameter space in each frame, \mathcal{P} ; (a) sawtooth, (b) sinusoid, (c) square wave, (d) triangle, and (e) noise. The color scheme for this figure has been altered to provide the highest contrast in both color and grayscale reproduction, where dark (black) represents the highest values of $\bar{\alpha}_c \eta$ and lightly colored (pink) represents the lowest values. The contours overlaid are from the surface plots of $\mathcal{V}(t)$ from Figure 4.

The results from Figures 4 and 9 show a general trend, mixing agrees with EI predictions that high period, high ϵ generally produce the optimal mixers.

Although some of the features of the mixing are captured, there are new features which need to still be explained, which is the continuing focus of this study, to provide better tools for predicting mixing quality in the most economical computational manner.

One key feature that is shown from the Lagrangian result and not supported by the Eulerian prediction is that a “leading edge” is always observed in the parameter space. This can most clearly be seen in the case of the sawtooth time dependence, shown in Figures 4(a) and 9(a). The thin

enhanced region of the parameter space near the upper left-hand corner suggests a very good mixer exists. In fact, it is the optimal mixing configuration because it shows up earliest as the best mixer when simulations are run for shorter periods of time ($t_L < 100$). These very fast mixers are also shown in Figure 5(a) as the small group of points located in the farthest lower left-hand corner of the τ -bias plot (darkest dots).

One possible explanation, which has yet to be fully explored, is that particles in the fluid flow might be moving at exactly the same speed as $a(\omega t)$. In other words, when the velocity field is oscillating back and forth, there is a subset of fluid particles that move in exactly the same manner and speed as $a(\omega t)$. This will best be observed for a sawtooth time dependence of $a(\omega t)$ as those particles will be carried along with $a(\omega t)$ the farthest from the left gyre to the right gyres location, then suddenly, the sawtooth time dependence of $a(\omega t)$ returns back to its starting point, where it continues to move linearly back to its farthest right-hand position. The particles which move along with $a(\omega t)$ “co-move” such that they find themselves the deepest transported into the next gyres domain when $a(\omega t)$ returns, facilitating mixing for those specific configurations in the parameter space that co-move.

To understand why the other time-dependent functions show a less pronounced co-moving edge, consider how the double gyre changes in time. The triangular and sinusoidal time dependencies do not suddenly return back to the left-most position, such that any particles which are co-moving with $a(\omega t)$ are simply carried back towards the left-hand gyre, not suddenly deposited into the right-hand gyre’s domain. The square wave time dependence does change its velocity field abruptly, however, the rest of the time the velocity field is dormant, so there can be no co-moving particles along with $a(\omega t)$. Finally, the noisy time-dependent function shows no preference in the parameter space like the leading edge that is observed in the sawtooth, sinusoidal, square wave, and triangular time dependencies.

At present, no EI has been developed to measure the degree that a velocity field might co-move particles in the fluid. As such, the Lagrangian mixing quality properly shows this feature, where the EIs properly *fail* to show this feature. One further suggestion from the figure comes from the angle shown in the leading edge. For the sawtooth, the leading edge is clearly linear, suggesting that the ratio of the maximal displacement of the gyres, ϵ , divided by the period represents a “velocity” that the co-moving particles are exhibiting. The sinusoidal and triangular time dependencies show a broader leading edge, suggesting that the co-moving particles in the fluid are less distinct in the parameter space as the correlation between ϵ and the fluids particles movement is less strong. Despite the lesser correlation (wider distribution), the leading edges of the parameter space for the sinusoidal and triangular cases do correlate with a higher slope than the sawtooth time dependence, as should be expected from the slopes of the time dependence, where both triangular and sinusoidal waveforms have a higher slope than the sawtooth.

C. Computational efficiency

We have performed five sets of simulations, one for each time dependence. In each case, both particle trajectory based and Eulerian metrics were calculated. Also, for each case, the parameter space of T - ϵ , was studied at ~ 5000 positions at random locations. In some cases, more values of the parameter were used in order to provide the smoothest surfaces for illustration. The length of time used for a single simulation was $t_L = 100$ with a time step of $\Delta t = 0.1$. This length of time allows for the slowest period oscillations to complete 5 full oscillations before the simulation ended as well as allowing for asymptotic behavior to be exhibited.

EIs have been previously discussed (see Refs. 13, 15, and 16) as having a distinct advantage when studying dynamical systems in that they can *predict* some traits of the dynamics under study *without having to perform the costly computational steps of integrating velocity vector fields to obtain trajectories*. How efficient are EIs? A typical calculation on a 6-core 2.5 GHz workstation filling in a parameter space of T - ϵ with 5000 configurations performed on a 200×100 grid of initial particle locations with a simulation final time of $t_L = 100$ would take ~ 4 hours, or 14 400 s, or 86 400 s/core. To perform the Lagrangian study of integrating the trajectories in order to obtain the variance of concentration for the same conditions would typically take 4 days, running over

30-cores on a variety of machines with a average speed of 2.2 GHz, resulting in 10 368 000 s/core. This means the Eulerian calculation runs $\sim 108:1$ times faster than the Lagrangian calculation. In each case, MATLAB was the programming environment, using a 4th order Runge-Kutta algorithm to perform the integration steps.

VI. CONCLUSIONS AND OUTLOOK

In this paper EIs were generalized and developed for continuously time varying two-dimensional flows. In previous work,^{15,16} EIs were developed for the discrete time (“blinking”) case. The EI quantifying “streamline crossing” (which we refer to as “transversality”, $\bar{\alpha}_c$) and mobility, η have been generalized from the discrete time case. For the continuously time varying case the rate of temporal variation of the velocity field (at any given point in the flow domain) is quantified by a new EI, the RROC and its associated spatial average, ζ . The RROC is used in the continuous time definition of the mobility.

The effectiveness of the EIs for predicting the regions in parameter space corresponding to the “best” mixing is studied by considering the time-dependent double-gyre model of Shadden *et al.*¹⁷ with five different time dependencies: sawtooth, sinusoidal, square wave, triangular, and noise. Each time-dependent velocity field is described by two parameters, T - ϵ , where a systematic study of mixing was carried out for the range $1 \leq T \leq 20$, $0 \leq \epsilon \leq 0.5$, with ~ 5000 parameter values in this range considered for each time dependence.

The particle trajectory based mixing diagnostic used to assess the quality of mixing and compared with the EIs is the time-dependent variance of concentration. This was calculated for a time of $t_L = 100$ units since it was determined that for this length of time, all of the model configurations reach their asymptotic values for the variance of concentration. Over this time interval the variance of concentration was fitted to an exponential depending on two parameters, τ and *bias*. In the τ – *bias* plane, the distinction between the mixing quality is largely determined by the *bias* value and not τ . A high *bias* value suggests the presence of island structures creating barriers to particle transport and full mixing. This observation follows for each of the five time dependences. We found that there are two hierarchies of mixing: the hierarchy of the best mixing values and the hierarchy of the largest parameter space coverage for the best mixing. The best mixing values show that the triangular time-dependence is the fastest and most thorough mixer as can be seen from Figure 5(d). The rest of the hierarchy is (from best to worst time dependencies): triangular, sinusoidal, square wave, sawtooth with noisy being the worst mixing time dependence. The best mixing based on the most coverage in the plane of T - ϵ from best to worst is: noisy, sawtooth, square wave, triangular with the worst parameter space coverage by the sinusoidal time dependence. Each time dependence exhibits a plateau in the T - ϵ parameter space which correspond to the best mixing configurations. We found that the EI product of transversality and mobility, $\bar{\alpha}_c \eta$, is correlated with the plateau in the parameter space corresponding to the best mixing.

ACKNOWLEDGMENTS

The research of S.W. was supported by Office of Naval Research (ONR) Grant No. N00014-01-1-0769 and the research of K.M. was supported by Office of Naval Research (ONR) Grant No. N00014-09-WR-2-0256.

APPENDIX A: CONSTRUCTION OF A VELOCITY FIELD WITH CONTINUOUS, BUT NOISY, TIME DEPENDENCE USING THE RROC

In this appendix we describe how we construct the noisy time dependence of a velocity field. In Sec. III B we showed that the RROC can be used as a measure of how quickly a function is changing in time, and this can then be used to characterize a “frequency” for noise. This provides us with a method for computing a noisy, but periodic function, that we now describe. For the initial discussion, a scalar valued function of time only will be used, however, the general definition of the RROC is applicable to vector valued functions as defined by Eq. (20). Recalling from Sec. III B

TABLE I. Table of ratio of RROC between the various time dependencies. Note that the noise ratio is a limit imposed by the process of smoothing the function.

Time dependence frequency	Ratio of RROC to frequency ($1/T$) RROC/ f
Square wave	2
Sawtooth	6.16
Sinusoidal	10.44
Triangular	11.10
Noise	≤ 10

(Eqs. (18)–(20)), but rewriting the equations for the RROC in one dimension for simplicity,

$$\Delta w(t, \Delta t) = \frac{|f(t + \Delta t) - f(t)|}{|f(t + \Delta t)| + |f(t)|}, \quad (\text{A1})$$

$$dw = \lim_{\Delta t \rightarrow 0} \Delta w(t, \Delta t), \quad (\text{A2})$$

$$(\text{RROC}) \tilde{w} = \frac{1}{t_E} \int_0^{t_E} dw, \quad (\text{A3})$$

where t_E is chosen to be an integral multiple of T , mT , where m has the property that it is the largest integer such that $mT \leq 20$, $(m + 1)T > 20$. The RROC measures a maximal change whenever a function of time changes sign from one point in time to the next. For the discrete time case, where time is measured in steps of Δt , the relative change, $\Delta w(t, \Delta t)$ measures a relative distance between any two consecutive values which has a range from zero to one provided the two values have the same sign. As soon as one value has a different sign from the other, the relative change becomes one. In this sense, the relative change acts as a counter for how often a time varying function changes sign. For a simple periodic function, this should occur exactly two times per period. By summing the relative change over a full period, a minimum value of two should be obtained for periodic functions. In addition to the minimal value of two units for each period, any additional changes that occur when two consecutive values are the same sign will depend on how different the values are from each other. When a function varies slowly over time, the relative difference is small, whereas, for a fast varying function in time, the slope of the function will cause this additional relative change to increase. The summation of all relative changes over a periodic function is sensitive to how often the function changes sign as well as how high the slope of the function becomes.

The square wave has an exact value of the relative change of two per period, as it has two sign changes and zero relative change in between changing signs. In this specific case, by dividing by the period of the square wave, the ratio of the summed relative change to the period is exactly twice the frequency of the square wave. The ratio of the integrated relative change to the period is the relative rate of change, the RROC. In comparison, periodic functions with high slopes will have a higher value for the RROC, and lesser slopes will have a lower RROC, yet still higher than two. In order from highest to lowest, the triangular time dependence is highest followed closely by the sinusoidal, nearly half-way in between is the sawtooth (it has half the slope of the triangular) and at the minimal value is the square wave time dependence. From lowest to highest, the relative rate of change is: square wave, sawtooth, sinusoidal then triangular. The triangular and sinusoidal are almost tied for the highest value. Table I shows the ratio of the RROC for the time dependencies studied relative to the frequency ($f = 1/T$). One can use the RROC to construct a function with features similar to another time varying function simply by creating a function in time, $f(t)$, whose RROC is similar to one of the functions listed above. The easiest function to mimic is a sinusoid. In order to demonstrate this, a noisy function was generated by using a random number generator between $\pm \text{Amp}_0$ for every time step from $i = 1 \rightarrow N$. This initial noisy function has a very high value for the RROC. For a given period of time, the RROC is computed for this noisy function. The function is then smoothed

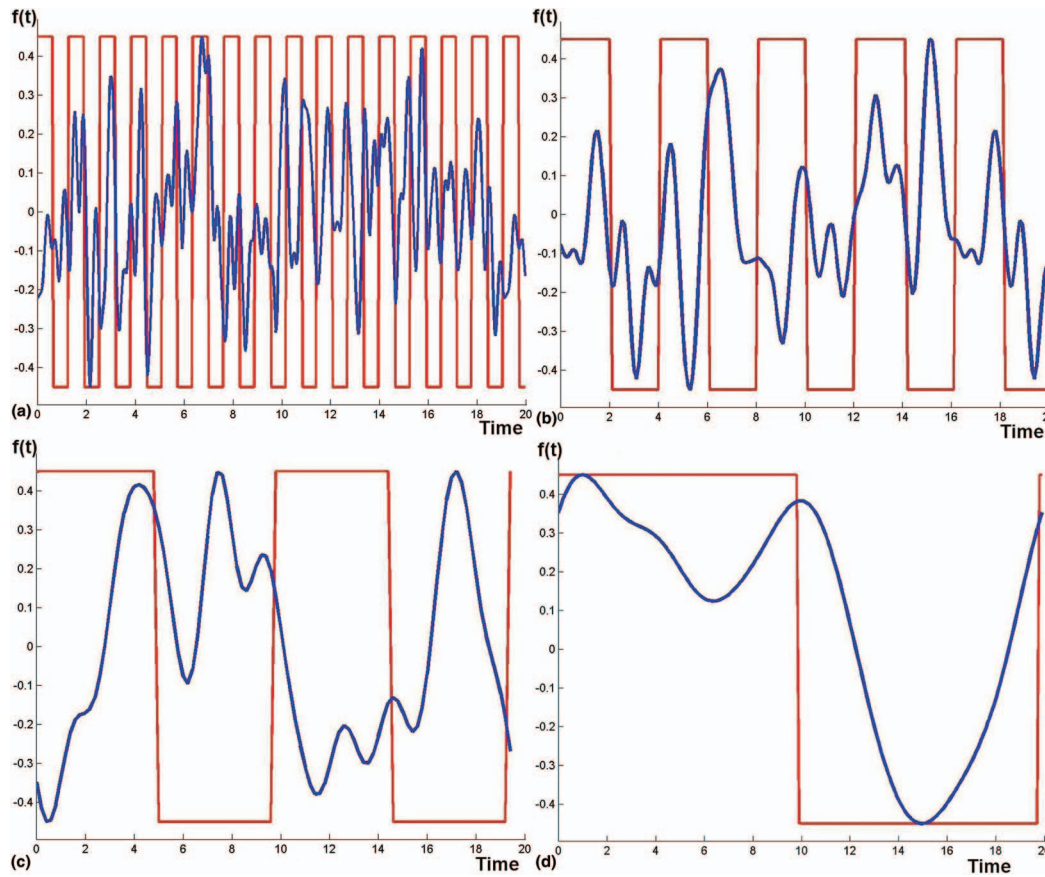


FIG. 10. Four noisy functions, smoothed until the ratio of the RROC to the frequency drops below 10.0. Periods for each frame are: (a) $T_1 = 1.27$, (b) $T_2 = 4.03$, (c) $T_3 = 9.66$, and (d) $T_4 = 19.8$.

by averaging the value at $f(t)$ with $f(t+\Delta t)$. The function can be made cyclic by setting the value $f(t_{N+1}) = f(t_1)$. For the examples shown below, $N = mT$, where the period, T , was chosen such that the function would repeat every mT iterations, with m equal to a positive integer. In this manner, for the examples shown in Figure 10, differing periods can be compared ranging from $1 \leq T \leq 20$. For the case when $m > 1$, the value of the RROC must account for the multiple periods in the time window by setting the final time to include the multiple periods

$$(\text{RROC})\tilde{w} = \frac{1}{t_E} \int_0^{t_E} dw, \quad (\text{A4})$$

where $t_E = mT$, $m \geq 1$.

Each time the function is smoothed, the amplitude must be increased such that the function remains between $\pm \text{Amp}_o$. With each smoothing operation, the value of the RROC decreases as the smoothing process removes higher frequency components from the function. This process of computing the RROC and smoothing, then re-scaling continues until the RROC drops below a fixed value, a threshold. Using the value of $10f_w$ as the threshold for the RROC to drop below ($10f_w$ is characteristic of the RROC for a sinusoid), the noisy function becomes smoother, while retaining its initial randomness. The chosen time window, $0 \leq t \leq mT$, determines the time scale on which the noisy function begins to repeat itself. Because the function used is cyclic, the smoothed noisy function is guaranteed to be matched at the time $t_E = mT$.

Below is shown an algorithm for generating noise of the type shown in this paper.

1. “Seed” a random function with a large number of samples, $N \gtrsim 100$ points.
2. Smooth the function:

$$f(t) = [f(t_1), f(t_2), f(t_3), \dots, f(t_i), \dots, f(t_N)],$$

$$f(t + \Delta t) = [f(t_2), f(t_3), f(t_4), \dots, f(t_{i+1}), \dots, f(t_1)],$$

$$f_{smooth}(t) = \frac{1}{2}[f(t) + f(t + \Delta t)],$$

$$f_{rescaled} = \frac{2Amp_o}{f_{max} - f_{min}}[f_{smooth} - \langle f_{smooth} \rangle].$$

3. Calculate the RROC, \tilde{w} .
4. If $\tilde{w} > threshold$, re-smooth (*Go to step 2*).
5. If the number of smoothing operations is one or less, re-seed (*Go to step 1*).
6. Done.

Figures 10(a)–10(d) illustrate the process by showing four different noisy functions with differing periodicities. A square wave is also shown which has the same period as the four different noisy functions. The periods for each function are approximately $T_i = 1, 4, 10$, and 20 , respectively. In each of the cases shown, the RROC was calculated for the time window from $t \in [0, mT_i]$, however, the function was allowed to continue until a common end time, $T_{final} = 20$, so that a comparison can be made between the various noisy functions.

APPENDIX B: A CHARACTERISTIC TIME SCALE FOR THE FLOW

From Sec. III C, the definition of mobility is intimately tied to the idea that transport can occur when a particle in a fluid is given sufficient time to move within the domain to new areas, where the velocity field changes enough such that the particle is taken “away” from the initial region from which it started. To this end, a velocity vector field that oscillates in time runs the risk of changing direction back and forth in such a way that particles do not effectively transport away from where they begin. In Sec. III C, two different quantities, v_{fast} and v_{slow} , were defined such that if a velocity field changes directions too “quickly,” a particle effectively becomes trapped in that region of space, as no clear direction is ever established for the particle to move in, in other words, it oscillates with little net displacement. When a velocity field changes “slowly,” a particle in the fluid should be able to transport away from the region it is in, provided the magnitude of the velocity field is sufficient. By setting a threshold velocity, the EI for mobility measures the percentage of a domain that provides effective transport within the domain. In order to properly interpret the conditions that a velocity vector field is changing “quickly or slowly” enough, two values are required, a rate of change and a time-scale. Section III B and Appendix A have shown how to determine a rate of change for a velocity field. This appendix will define a characteristic time-scale which is used in the definition for the mobility, shown in Eq. (25).

Figure 11 shows a single gyre velocity field with no-slip boundary conditions. For this case, the magnitude of the velocity field will be zero along all the domains walls as well as zero at the gyre’s center. The maximal velocity is found along trajectories approximately half-way between the gyre center and the walls. A characteristic time will be defined by first finding the angular velocity for the fastest moving particles.

First, define a characteristic length scale as half of the distance from the center of the domain to one of the corners divided by two and divided by the number of gyres in the domain

$$L_{char} = \frac{\sqrt{\frac{L_x^2}{2} + \frac{L_y^2}{2}}}{2N_{gyres}}. \quad (B1)$$

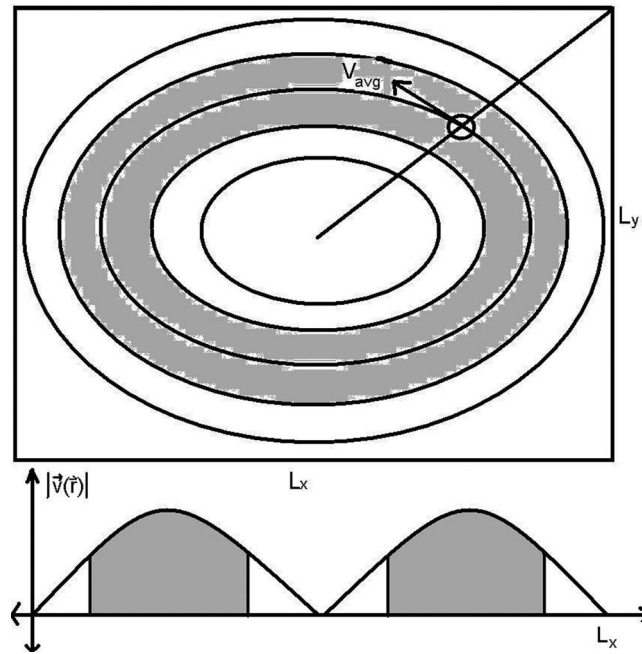


FIG. 11. Sketch illustrating how a characteristic time-scale can be determined for a single gyre in a typical flow (only a single gyre is shown, for clarity).

This definition of a length scale is appropriate when working with a large number of gyres distributed over the domain.

Second, define a velocity magnitude which characterizes the main part of the fluid's flow, in other words, ignoring those regions where the magnitude is close to zero (the center of the gyre and near the no-slip walls). For the average velocity, take the average of the upper half of the velocity fields magnitudes, as this value will represent the average velocity that is engaged in the flow

$$v_{avg} = \frac{1}{N} \sum_{i=1}^N |\mathbf{v}(\mathbf{r}_i)|, \quad |\mathbf{v}_i| > 0.5v_{max}. \quad (\text{B2})$$

Define the angular velocity as

$$\omega = \frac{v_{avg}}{L_{char}}. \quad (\text{B3})$$

Finally, define the time-scale as the length of the time taken by particles flowing in the domain to complete one revolution

$$T_{\text{revolution}} = \frac{2\pi}{\omega}. \quad (\text{B4})$$

The “characteristic time-scale” for use with the EI for mobility should represent a time-scale appropriate for transport away from a region in the velocity vector field's domain. But waiting long enough for one full revolution to occur is too long for this purpose. For this study, the *characteristic time*, T_c was set to be one half of a full revolution's time, as this still allows significant transport to occur along both the vertical as well as horizontal directions

$$T_c = \frac{1}{2} T_{\text{revolution}}. \quad (\text{B5})$$

The characteristic time found for this study, which has two gyres, was $T_c = 4.132$.

It is worth noting that this is simply a choice to define a reasonable time-scale for this particular model's velocity vector field. Other boundary conditions and other models will probably have other time-scales that are defined differently and are more appropriate to those models/conditions.

The important value to obtain is *some reasonable time-scale*. The method is not as important as establishing the time-scale that is sensitive to the dynamics under question. More generally, in order to properly define the EI for mobility, any rate and time-scale can be used – so long as the rate and time-scale are appropriate to the motions under consideration.

- ¹ O. Reynolds, “Study of fluid motion by means of coloured bands,” *Nature (London)* **50**, 161–164 (1894).
- ² C. Eckart, “An analysis of the stirring and mixing processes in incompressible fluids,” *J. Mar. Res.* **7**(3), 265–275 (1948).
- ³ P. V. Danckwerts, “The definition and measurement of some characteristics of mixtures,” *Appl. Sci. Res.* **A3**, 279–296 (1952).
- ⁴ P. V. Danckwerts, “Theory of mixtures and mixing,” *Research* **6**, 355–361 (1953).
- ⁵ J. M. Ottino, S. C. Jana, and V. S. Chakravarthy, “From Reynolds’s stretching and folding to mixing studies using horseshoe maps,” *Phys. Fluids* **6**(2), 685–699 (1994).
- ⁶ J. M. Ottino, “Mixing, chaotic advection, and turbulence,” *Annu. Rev. Fluid Mech.* **22**, 207–254 (1990).
- ⁷ E. Villermaux, A. D. Stroock, and H. A. Stone, “Bridging kinematics and concentration content in a chaotic micromixer,” *Phys. Rev. E* **77**, 015301(R) (2008).
- ⁸ S. Wiggins and J. M. Ottino, “Foundations of chaotic mixing,” *Philos. Trans. R. Soc. London* **362**(1818), 937–970 (2004).
- ⁹ J. M. Ottino and S. Wiggins, “Designing optimal micromixers,” *Science* **305**, 485–486 (2004).
- ¹⁰ R. Sturman, J. M. Ottino, and S. Wiggins, *The Mathematical Foundations of Mixing*, Cambridge Monographs on Applied and Computational Mathematics Vol. 22 (Cambridge University Press, Cambridge, 2006).
- ¹¹ H. Aref, “Stirring by chaotic advection,” *J. Fluid Mech.* **143**, 1–21 (1984).
- ¹² D. V. Khakhar, J. G. Franjone, and J. M. Ottino, “A case study of chaotic mixing in deterministic flows: The partitioned pipe mixer,” *Chem. Eng. Sci.* **42**, 2909–2926 (1987).
- ¹³ R. Sturman and S. Wiggins, “Eulerian indicators for predicting and optimizing mixing quality,” *New J. Phys.* **11**, 075031 (2009).
- ¹⁴ A. D. Stroock, S. K. W. Dertinger, A. Ajdari, I. Mezic, H. A. Stone, and G. M. Whitesides, “Chaotic mixer for microchannels,” *Science* **295**, 647–651 (2002).
- ¹⁵ K. McIlhany and S. Wiggins, “Optimizing mixing in channel flows: Kinematic aspects associated with secondary flows in the cross-section,” *Microfluid. Nanofluid.* **10**, 249–262 (2011).
- ¹⁶ K. L. McIlhany, D. Mott, E. Oran, and S. Wiggins, “Optimizing mixing in lid-driven flow designs through predictions from Eulerian indicators,” *Phys. Fluids* **23**(8), 082005 (2011).
- ¹⁷ S. C. Shadden, F. Lekien, and J. E. Marsden, “Definition and properties of Lagrangian coherent structures from finite-time Lyapunov exponents in two-dimensional aperiodic flows,” *Physica D* **212**(3–4), 271–304 (2005).
- ¹⁸ M. Funakoshi, “Chaotic mixing and mixing efficiency in a short time,” *Fluid Dyn. Res.* **40**, 1–33 (2008).